Pseudocapacitive Energy Storage and Electrocatalytic Hydrogen-Evolution Activity of Defect-Ordered Perovskites $Sr_xCa_{3-x}GaMn_2O_8$ (x = 0 and 1)

Surendra B. Karki[1], Farshid Ramezanipour[1,*]

[1]Department of Chemistry, University of Louisville, Louisville, Kentucky 40292, USA

*Corresponding author. Email: farshid.ramezanipour@louisville.edu, Phone: +1(502) 852-7061

ORCID iD: 0000-0003-4176-1386

Abstract

The diverse range of possible arrangements of oxygen-vacancies in oxygen-deficient perovskites results in a variety of structure types and fascinating electrochemical properties. Here, we report $Ca_3GaMn_2O_8$ and $SrCa_2GaMn_2O_8$, where the ordering of oxygen-vacancies leads to cation and polyhedral order, resulting in a remarkable array of electrochemical properties coexisting in the same compound. Neutron and X-ray diffraction have been utilized to study the structure of these materials that feature simultaneous defect-order and cation-order. Remarkably, both materials show very high electrocatalytic activity for hydrogen-evolution reaction (HER) of water-splitting in bulk form, without the need for composite formation or nanofabrication. The HER overpotential required to achieve a current density of 10 mA/cm^2 is as low as $\eta_{10} \approx$ -315 mV. In addition, detailed pseudocapacitive studies show that both compounds are capable of energy-storage as anion-based pseudocapacitors, arising from oxygen ion intercalation. The symmetric pseudocapacitor cells fabricated based on these materials show a combination of high energy density and power density. These pseudocapacitor cells are also extremely stable, maintaining their high activity over 1000 cycles of charge-discharge. Electrical charge-transport studies indicate that these compounds have semiconducting properties in a wide temperature range, 25 – 800 °C. Magnetic studies using both magnetometry and neutron scattering indicate a transition to an antiferromagnetic state, with a G-type arrangement of spins, where the moment on each Mn is aligned anti-parallel to all nearest neighbors. This combination of properties indicates the great potential of this class of defect-ordered systems and their importance to energy research.

Keywords: Pseudocapacitor; Hydrogen-evolution reaction; Oxide; Ordering; Stability

1. INTRODUCTION

The discovery of new materials that possess electrochemical properties suitable for development of renewable energy systems is essential. Properties such as electrical conductivity and charge storage are important to the operation of different systems such as fuel cells, batteries, and supercapacitors.

In recent years there has been considerable effort dedicated to the discovery of catalysts for water splitting,[1-4] which are motivated in part by the high cost of precious metal catalysts.[5] While platinum is an excellent catalyst for hydrogen evolution reaction (HER), the search for more economical catalysts has led to the investigation of a wide range of compounds from carbides[1] to borides,[2] sulfides,[3] chalcogenides,[4] and oxides.[6] Similarly, various classes of compounds[7-10] have been explored for the oxygen-evolution reaction (OER), such as oxides,[7-8] sulfides[9] and various nanomaterials and composites.[10]

In recent years, material discovery efforts have also been directed to finding new materials for intercalation-based pseudocapacitors,[11] in particular those involving oxygen ion intercalation, which was first shown in $Nd_{1-x}Sr_xCoO_3$.[12] A number of oxide materials including $LaMnO_3$,[11] $La_{1-x}Sr_xMnO_3$,[11, 13-14] $La_{1-x}Ca_xMnO_3$,[15] $SrCo_{0.9}Nb_{0.1}O_3$,[16], and $LaNi_{1-x}Fe_xO_{3-\delta}$[17] have been studied for oxygen anion intercalation.

Among different classes of functional materials, the perovskite-based oxides, in particular those derived from oxygen-deficient perovskites, show a wide range of interesting properties, which can be utilized for energy applications. In these $ABO_{3-\delta}$ type materials, oxygen-deficiencies result in different coordination geometries for the B-site cations, ranging from octahedral to tetrahedral and square pyramidal.[18] The oxygen-vacancies are sometimes distributed randomly.[19] There are also situations where the arrangement of oxygen-vacancies is ordered.[18] One of the

common types of ordering results in the so-called brownmillerite structure, named after mineral Ca_2AlFeO_5. The structure consists of sequential layers of tetrahedra (T) and octahedra (O), forming TOTOT…, with A-site cation residing between the layers. The tetrahedra form chains that are twisted in either left-handed or right-handed orientation to yield several orthorhombic structural variants adopting space groups such as *Ibm2*, *Pnma*, *Pbcm* or *Icmm*.[18, 20] The variation in the arrangement of oxygen-vacancies and the subsequent structural characteristics result in different types of properties.

For example, the oxygen-deficient perovskites $Sr_2Fe_2O_{6-\delta}$ and $CaSrFe_2O_{6-\delta}$ show different types of vacancy-order, resulting in significantly different electrical charge-transport. $Sr_2Fe_2O_{6-\delta}$ shows a persistent decrease in electrical conductivity as a function of temperature, whereas $CaSrFe_2O_{6-\delta}$ exhibits an increase followed by a decrease in conductivity in the same temperature range.[18] In addition, magnetic properties change significantly. In $Sr_2Fe_2O_{6-\delta}$, an incommensurate magnetic structure is observed[21] where moments are in spin-density wave state and are oriented perpendicular to the body diagonal of the unit cell. Whereas, $CaSrFe_2O_{6-\delta}$ shows long-range antiferromagnetic order, where the moments align in 001 direction.[18] Another example is the effect of vacancy-order on sensor properties for oxygen, carbon dioxide, and carbon monoxide sensing using oxygen-deficient perovskites.[22] Furthermore, the electrocatalytic activity is significantly affected by structure and ordering scheme, as shown recently for a series of oxygen-deficient perovskites.[7]

While the brownmillerite type ordering is commonly observed, there is also a similar, but less common ordering scheme with ideal formula $A_3B_3O_8$ ($ABO_{3-(1/3)}$), sometimes called Grenier phase.[23] This structure consists of bilayer stacks of octahedra alternating with a single layer of

tetrahedra, i.e., TOOTOOT…, often adopting orthorhombic space groups such as *P2$_1$ma*, *Pbma,* *Pmma,* and *Pb2$_1$m*.[24-27]

The tetrahedral layer consists of corner-sharing tetrahedral units that form parallel chains. The space group symmetry depends on the relative orientation of these chains. The *P2$_1$ma* space group adopts the cooperative twisting of tetrahedral chains in the same direction.[24] When the left-handed and right-handed orientations of tetrahedral chains alternate between adjacent layers of tetrahedra, the structure crystallizes in *Pbma* space group.[25] Finally, in *Pmma* space group, each tetrahedral chain orients opposite to all nearest neighbors within the same layer and in the neighboring layers above and below.[26] Few studies of the properties of this class of oxides have been conducted before.[28-29] The structure and magnetoresistance of a material with composition $Ca_{2.5}Sr_{0.5}GaMn_2O_8$ has been studied,[30] but no other information has been reported. The same authors also attempted to make $Ca_3GaMn_2O_8$, but could not obtain a pure phase.[30] In the present study, we report the synthesis, crystal structure, electrical conductivity, magnetic properties, electrocatalytic activity, and pseudocapacitive performance of two TOOTOOT… compounds, $Ca_3GaMn_2O_8$ and $SrCa_2GaMn_2O_8$, and show that these two materials demonstrate a remarkable combination of electrochemical properties that coexist in the same compound.

2. EXPERIMENTAL

2.1. Materials Synthesis

Polycrystalline samples of $Ca_3GaMn_2O_8$ and $SrCa_2GaMn_2O_8$ were synthesized through a solid-state synthesis route using powders of $CaCO_3$, $SrCO_3$, Ga_2O_3, and Mn_2O_3. The precursors in stoichiometric ratios were mixed using an agate mortar and pestle and pressed into pellets. The

pellets were calcined at 1000 °C for 12 hours in air. The samples were then reground, re-pelletized, and sintered at 1100 °C for a total of 72 hours in air, which included two intermediate grindings. The heating and cooling rates of the furnace for all samples were 100 °C/hour.

2.2. Materials Characterization

$Ca_3GaMn_2O_8$ and $SrCa_2GaMn_2O_8$ were structurally characterized using a high-resolution Cu Kα1 X-ray diffractometer (λ = 1.54056 Å). Rietveld refinements were carried out using the GSAS [31] software and EXPEGUI [32] interface. The morphological analyses were performed using high-resolution field-emission scanning electron microscopy (SEM). Iodometric titration under argon atmosphere was performed to determine the oxygen content of both materials. 50 mg sample and ~ 2g KI were dissolved into 100 mL of 1M HCl solution that had been purged with argon for 30 minutes before use. This solution was further degassed with argon for few minutes and stored under argon at least 12 hours to allow the reduction of metal ions. Then 5 mL of this stock solution was titrated under argon with 0.025M $Na_2S_2O_3$, where 5 - 10 drops of starch were added near the endpoint as an indicator.

The variable temperature (25 – 800 °C) electrical conductivity measurements in air were done using a four-probe DC technique on rectangular pellets. Current values were recorded by applying a potential of 0.01 V. Magnetic measurements were done on a vibrating sample magnetometer (VSM) to obtain magnetic susceptibility data at the temperature range of 2 – 400K, and isothermal magnetization data in fields up to 9 T. Neutron diffraction experiments at 10 K were performed on POWGEN diffractometer at Oak Ridge National Laboratory.

2.3. Electrocatalytic Characterization

The catalyst ink for hydrogen-evolution reaction (HER) and oxygen-evolution reaction (OER) was prepared by bath sonicating 35 mg of the sample, 7 mg of carbon black powder (Fuel Cell Store), 40 µL Nafion® D-521 solution (Alfa Aesar, 5% w/w in water and 1-propanol) and 7 mL of THF (Alfa Aesar, 99%) for 15 minutes. The glassy carbon electrode (GCE) (5 mm diameter, 0.196 cm^2 area, HTW Germany) was polished with 5 µm and 0.3 µm aluminum oxide polishing solution (Allied Hightech Products Inc.) on a polishing cloth, sonicated for 3 minutes in ethanol (Decon Labs, Inc.) and finally washed with deionized water before use. Then, the catalyst ink (40 µL) was drop-casted on the surface of the GCE and left to dry in air overnight before running electrochemical experiments. The electrochemical studies were performed in a standard three-electrode cell using a rotating disk electrode (Pine Research Instruments) at 1600 rpm and SP-200 potentiostat (BioLogic Science Instruments). A commercial platinum electrode (Pine Research Instruments) was used as a counter electrode. The OER experiments were done in 0.1 M KOH solution using Ag/AgCl reference electrode in 3M NaCl (ALS Co., Ltd, Japan). The HER experiments were conducted in 0.1 M KOH, 1 M KOH, and 0.5 M H_2SO_4 with Ag/AgCl in saturated KCl as a reference electrode. Chronopotentiometry at -10 mA/cm^2 was employed for the HER stability test using the same catalyst ink loaded on GCE in the same HER electrolyte. The potential values were iR corrected, and then converted into potential versus reversible hydrogen electrode (RHE) using $E_{vs\ RHE} = E_{vs\ Ag/AgCl} + 0.059pH + E^0_{Ag/AgCl}$, where $E^o_{Ag/AgCl}$ = 0.21 V for 3M NaCl[33] and 0.197 V for saturated KCl.[34]

2.4. Pseudocapacitance Measurements

For pseudocapacitance studies, the same ink preparation method as above was used for three-electrode cyclic voltammetry (CV) measurements. In the three-electrode cell, the sample ink (40 μL) loaded on GCE was used as a working electrode, Pt as a counter electrode, and Ag/AgCl (in 3M NaCl) as a reference electrode to record CVs by scanning from -1.0 to 0.4 V (vs Ag/AgCl) using rotating disk electrode at 1600 rpm. Pt electrode was cleaned before use by bath sonicating for 15 minutes in 0.5M H_2SO_4.

For the fabrication of a symmetric two-electrode cell for galvanostatic charge/discharge (GCD), 100 μL of the same ink was pipetted in 20 μL increments to drop-cast onto both sides of a 1 cm^2 nickel foam followed by air-drying overnight. Two identical Ni foam electrodes with a total of 1 mg loading of active material were prepared. The two nickel foam electrodes were separated by placing a glass fiber filter paper between them. Gold wires and leads were clipped onto the electrodes to complete the cell circuit for studying GCD in 1 M KOH. The cell was soaked in 1 M KOH for at least an hour before GCD experiment and at least 12 hours before the stability test. The cell was used to record GCD curves at 0.5, 1, 3, 5, and 10 A/g current density. The GCD curves were recorded from 0.0 to 1.4 V vs Ag/AgCl stored in 3M NaCl (ALS Co., Ltd, Japan).

3. RESULTS AND DISCUSSION

3.1. Crystal Structure

The two compounds, $Ca_3GaMn_2O_8$ and $SrCa_2GaMn_2O_8$, belong to a defect-ordered family of oxides. Their crystal structures were determined by Rietveld refinements using powder X-ray

diffraction. Figure 1 shows the refinement profiles of the two compounds and Tables 1 and 2 lists the refined structural parameters. These compounds crystallize in the *Pcm2₁* space group, consistent with the structure of a similar compound, $Ca_{2.5}Sr_{0.5}GaMn_2O_8$, reported before.[30] Figure 2 shows the crystal structure and the distribution of cations, as well as the tetrahedral chain orientation for $Ca_3GaMn_2O_8$ and $SrCa_2GaMn_2O_8$. The structure of these materials is derived from the perovskite structure, as described in the introduction section. It is noted that regular perovskites (ABO_3) only contain AO_{12} and BO_6 polyhedra. However, the general formula for our compounds is $AA'_2B'B_2O_8$ (or $A_{1/3}A'_{2/3}B'_{1/3}B_{2/3}O_{3-1/3}$), indicating four distinct metal sites with different coordination geometries, namely AO_{12}, $A'O_8$, $B'O_4$, and BO_6 polyhedral units. This is a result of an ordering scheme (Figure 2), where oxygen-vacancies only appear in every third layer of a perovskite system, creating tetrahedral $B'O_4$ units that do not exist in a regular perovskite. This also results in the formation of 8-coordinated $A'O_8$ units. There are, therefore, two types of B-sites (Figure 2), namely octahedral (B=Mn) and tetrahedral (B'=Ga). There are also two types of A-sites: (a) 12-coordinated A=Ca sites located within bilayer MnO_6 stacks, and (b) 8-coordinated A'= Sr (or Ca for the Ca_3 phase) residing between MnO_6 octahedra and GaO_4 tetrahedra. As observed in Figure 2, the number of A' sites is twice the number of A positions. In $Ca_3GaMn_2O_8$, both A and A' sites are occupied by Ca. However, in $SrCa_2GaMn_2O_8$, the Sr atoms mostly reside in the A-site between neighboring MnO_6 layers, and most of the Ca atoms occupy the A' sites between GaO_4 and MnO_6 layers. The structure of $Ca_3GaMn_2O_8$ was also confirmed by neutron scattering, which showed magnetic peaks as well, and will be discussed further in the magnetic property section.

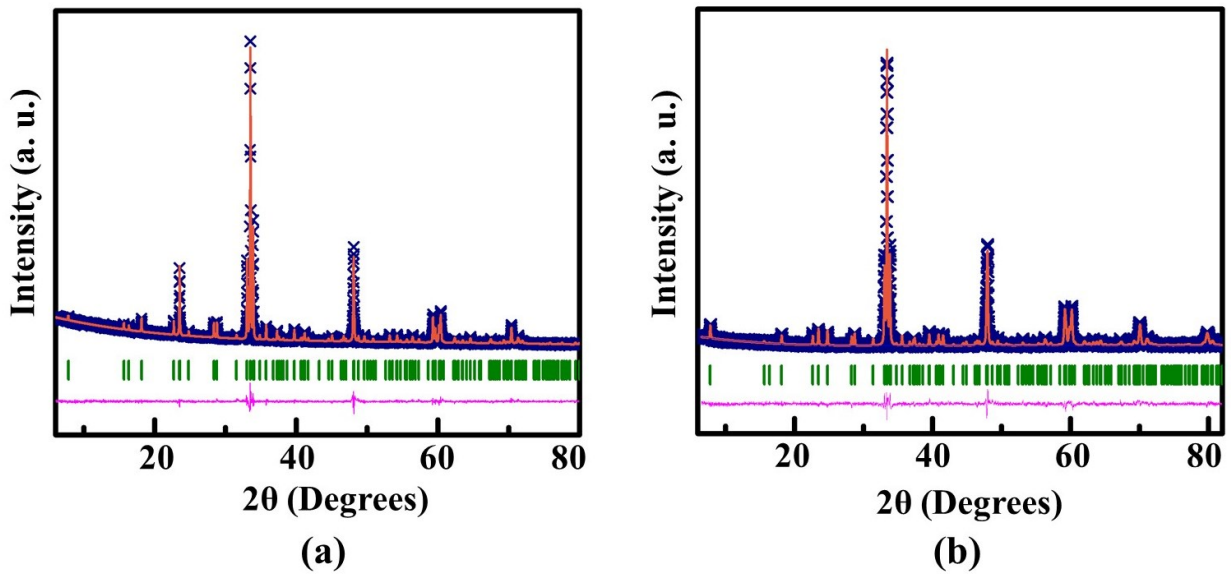

Figure 1. Rietveld refinement profiles of (a) $Ca_3GaMn_2O_8$ and (b) $SrCa_2GaMn_2O_8$ for powder X-ray diffraction data with space group $Pcm2_1$ (#26). The cross symbols, solid orange line, olive vertical tick marks, and lower magenta line correspond to experimental data, the calculated pattern for the $Pcm2_1$ model, Bragg peak positions, and difference plot, respectively.

Table 1: Refined structural parameters for $Ca_3GaMn_2O_8$ at room temperature using powder X-ray diffraction data. Space group: $Pcm2_1$, a = 5.4032(5) Å, b = 11.3013(4) Å, c = 5.2703(5) Å, R_p = 0.03459, wR_p = 0.04797.

Element	*x*	*y*	*z*	Multiplicity	Occupancy	Uiso
Ca1	0.224(1)	0.1881(5)	0.512(3)	4	1.0	0.021(3)
Ca2	0.245(1)	0.5	0.482(3)	2	1.0	0.014(3)
Ga1	0.316(1)	0.0	0.048(2)	2	1.0	0.029(3)
Mn1	0.2576(8)	0.3321(5)	0.0	4	1.0	0.021(2)
O1	0.393(7)	0.0	0.398(6)	2	1.0	0.10(2)
O2	0.298(3)	0.5	-0.013(7)	2	1.0	0.040(9)
O3	0.179(2)	0.139(1)	-0.025(5)	4	1.0	0.053(8)
O4	-0.008(5)	0.344(1)	0.245(8)	4	1.0	0.067(5)
O5	0.464(6)	0.299(1)	0.274(10)	4	1.0	0.047(8)

Table 2: Refined structural parameters for $SrCa_2GaMn_2O_8$ at room temperature using powder X-ray diffraction data. Space group: *Pcm2₁*, a = 5.4443(1) Å, b = 11.4387(2) Å, c = 5.31853(9) Å, R_p = 0.0212, wR_p = 0.0294

Element	*x*	*y*	*z*	Multiplicity	Occupancy	Uiso
Ca1/Sr1	0.2273(7)	0.1858(3)	0.509 (2)	4	0.85(1)/0.15(1)	0.047(2)
Ca2/Sr2	0.2429(6)	0.5	0.499(2)	2	0.40(2)/0.60(2)	0.031(2)
Ga1	0.317(1)	0.0	0.045(2)	2	1.0	0.054(3)
Mn1	0.2549(6)	0.3315(4)	0.0	4	1.0	0.043(2)
O1	0.387(6)	0.0	0.381(6)	2	1.0	0.13(2)
O2	0.294(3)	0.5	0.010(9)	2	1.0	0.068(8)
O3	0.175(2)	0.142(1)	-0.043(4)	4	1.0	0.048(6)
O4	0.004(5)	0.339(1)	0.257(8)	4	1.0	0.034(3)
O5	0.491(4)	0.3058(8)	0.256(8)	4	1.0	0.055(4)

Table 3. Selected bond distances and angles for $Ca_3GaMn_2O_8$ and $SrCa_2GaMn_2O_8$.

$Ca_3GaMn_2O_8$

Mn–O (Å)		Ga–O (Å)		Mn–O–Mn (degrees)	
Mn–O2	1.910(6)	Ga–O1	1.86(4)	Mn1–O2–Mn1	166.84(2)
Mn–O3	2.23(2)	Ga–O1	1.77(5)	Mn1–O4–Mn1	171.40(2)
Mn–O4	1.93(4)	Ga–O3	1.78(2)	Mn1–O5–Mn1	153.53(2)
Mn–O4	1.91(4)	Ga–O3	1.78(2)	Ga1–O1–Ga1	130.70(2)
Mn–O5	1.86(3)				
Mn–O5	1.95(3)				

$SrCa_2GaMn_2O_8$

Mn–O (Å)		Ga–O (Å)		Mn–O–Mn (degrees)	
Mn–O2	1.940(5)	Ga-O1	1.83(3)	Mn1–O2–Mn1	167.2(11)
Mn–O3	2.22(7)	Ga-O1	1.83(3)	Mn1–O4–Mn1	174.1(12)
Mn–O4	1.93(3)	Ga-O3	1.86(2)	Mn1–O5–Mn1	161.9(7)
Mn–O4	1.92(3)	Ga-O3	1.86(2)	Ga1–O1–Ga1	131.0(2)
Mn–O5	1.90(3)				
Mn–O5	1.92(3)				

All GaO_4 tetrahedra in these materials have the same orientation, arbitrarily assigned either right-handed or left-handed, throughout the structure, as shown in Figure 2c. There is an increase in the unit cell parameters of $SrCa_2GaMn_2O_8$ compared with $Ca_3GaMn_2O_8$ (Tables 1 and 2), which is expected given the larger ionic radius of Sr^{2+}.

The microstructure is also affected by the type of A-site cations. As shown in scanning electron microscopy (SEM) images in Figure 3, there is an increase in the size of crystallites for $SrCa_2GaMn_2O_8$ as compared with $Ca_3GaMn_2O_8$. The oxygen stoichiometry in these materials was also determined using iodometric titration, giving 8 oxygens per formula unit for both compounds, which matches the formulas of $Ca_3GaMn_2O_8$ and $SrCa_2GaMn_2O_8$.

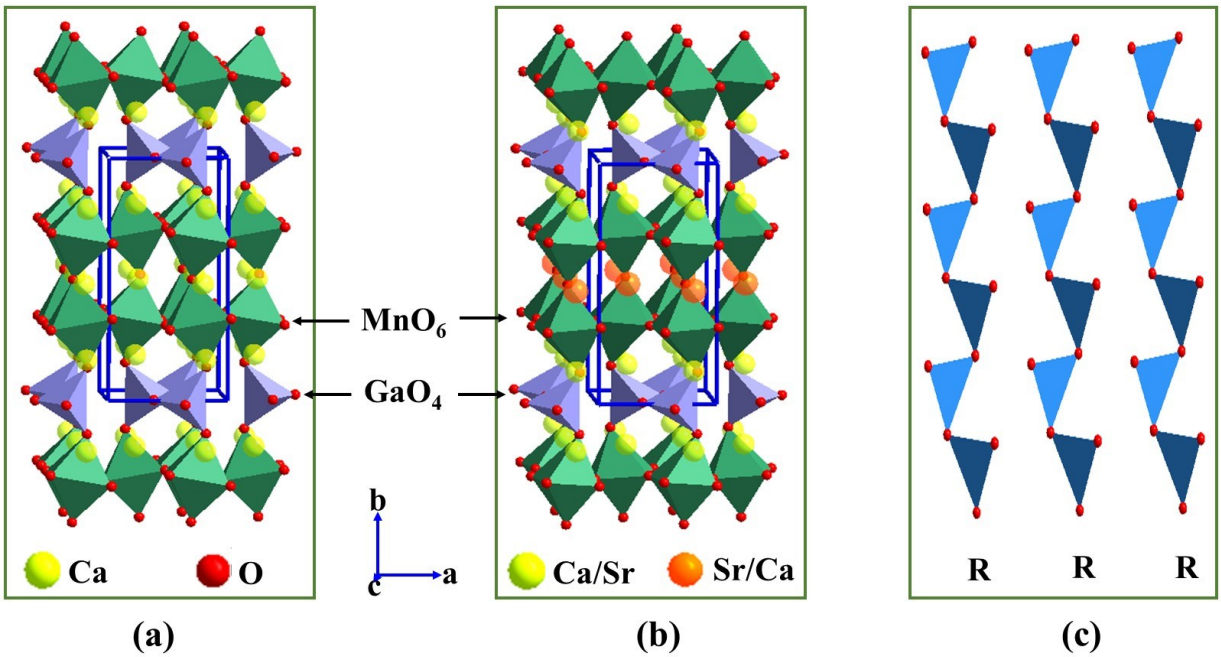

Figure 2. Crystal structures of (a) $Ca_3GaMn_2O_8$ and (b) $SrCa_2GaMn_2O_8$. Image (c) shows the relative orientation of tetrahedral chains in these compounds, viewed through the *b* axis.

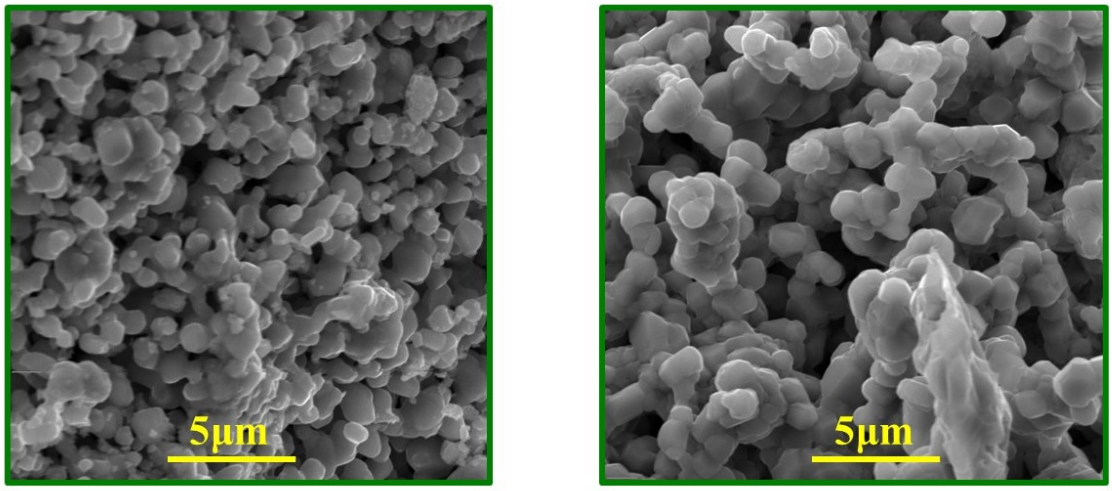

Figure 3. Scanning electron microscopy (SEM) images for sintered pellets of (a) $Ca_3GaMn_2O_8$ and (b) $SrCa_2GaMn_2O_8$.

3.2. Electrical Charge Transport

Variable temperature electrical conductivity was studied for both $Ca_3GaMn_2O_8$ and $SrCa_2GaMn_2O_8$ from 25 °C to 800 °C (298 K -1073 K). The current response from DC measurement is used to obtain the resistance using Ohm's law, which is then converted into conductivity (σ) using equation 1.[35]

$$\sigma = \left(\frac{I}{V}\right).\left(\frac{L}{wh}\right) \qquad (1)$$

where, I, V, L, w, and h are the current, applied potential, the distance between the voltage contacts in four-probe setup, width, and thickness of the rectangularly shaped sample, respectively. Figure 4a shows the variable-temperature conductivity data. $Ca_3GaMn_2O_8$ shows higher conductivity than $SrCa_2GaMn_2O_8$ in the whole temperature range. The electrical conductivity of both materials increases as a function of temperature, a behavior typical of semiconducting materials. The temperature-dependent increase in conductivity can be due to the increase in mobility of charge carriers as a function of temperature, described by equation 2.[36]

$$\sigma = n\, e\, \mu \qquad (2)$$

where σ is conductivity, n is the concentration of electrons/holes, e is the charge of the electron, and μ is the mobility of charge carriers. The activation energy (E_a) for the temperature-dependent increase in the conductivity of these materials can be calculated using the Arrhenius equation:[35]

$$\log \sigma T = \log A - \left(\frac{E_a}{2.303kT}\right) \qquad (3)$$

where *A*, *k*, and T represent the pre-exponential factor, Boltzmann constant, and temperature, respectively. Figure 4b shows the plot of log (σT) versus 1000/T. The activation energy is obtained using the slope from the linear fit to the data above 200 °C (473 K). The E_a values are equivalent to the slope multiplied by *k* value (8.62×10^{-5} eV. K^{-1}), 2.303, and 1000. The observed linear fit suggests that the conduction process obeys the Arrhenius law given by equation 3. The E_a values are consistent with the conductivity trend. $Ca_3GaMn_2O_8$, which shows higher conductivity, has lower activation energy. Whereas $SrCa_2GaMn_2O_8$ with lower conductivity shows higher activation energy.

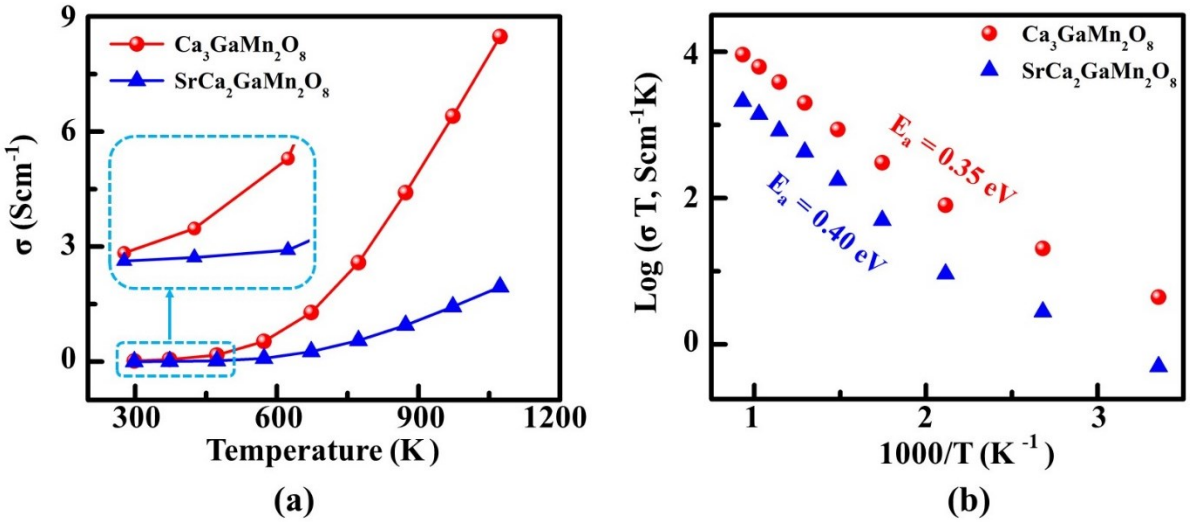

Figure 4. (a) Variable-temperature electrical conductivity, and (b) Arrhenius plots for the conductivity data of $Ca_3GaMn_2O_8$ and $SrCa_2GaMn_2O_8$.

The difference between the electrical charge transport of the two materials is due to the structural differences. In oxides, electronic conduction takes place through M^{m+}–O–M^{n+} pathway,[37] where M represents a transition metal with variable oxidation states.[36] In the two materials studied in this work, the presence of manganese atoms is repsosible for the conduction. It has been shown that the bond lengths and angles play an important role in conductivity. Shorter M–O bonds and more linear M–O–M angles lead to enhanced conductivity.[38] It appears that in this case, the effect of shorter bond length is dominant. While the bond angles in $SrCa_2GaMn_2O_8$ are closer to linear (Table 3), the Mn–O bond distances in $Ca_3GaMn_2O_8$ are slightly shorter. Furthermore, as observed from the SEM images in Figure 3, the grains in the sintered pellet of $Ca_3GaMn_2O_8$ are packed more closely, which can contribute to the enhanced conductivity.

3.3. Magnetic Properties

Zero-field cooled and field cooled magnetization data of $Ca_3GaMn_2O_8$ and $SrCa_2GaMn_2O_8$ are shown in Figure 5. The magnetization data reveal magnetic transitions below 120 K and 150 K, for $Ca_3GaMn_2O_8$ and $SrCa_2GaMn_2O_8$, respectively. The low values of magnetic susceptibility in the entire temperature range (2 K - 400 K), indicate that there is little uncompensated moment in both materials. This is further confirmed by isothermal magnetization data shown in Figure 5. These data reveal low magnetization values even at a magnetic field of 9 T at 2 K, where magnetization values reach a maximum of 0.19 μB and 0.10 μB per mole for $Ca_3GaMn_2O_8$ and $SrCa_2GaMn_2O_8$, respectively. These low magnetizations, along with the transition observed in magnetic susceptibility indicate that the magnetic state of these materials at low temperature is antiferromagnetic, which is also reported for a similar compound $Ca_{2.5}Sr_{0.5}GaMn_2O_8$.[30] The antiferromagnetic order in our materials was further confirmed by neutron scattering at 10 K for

$Ca_3GaMn_2O_8$. The magnetic structure was analyzed using GSAS software and EXPEGUI interface.[31-32] Figure 6a shows the Rietveld refinement profile with both magnetic and atomic phases.

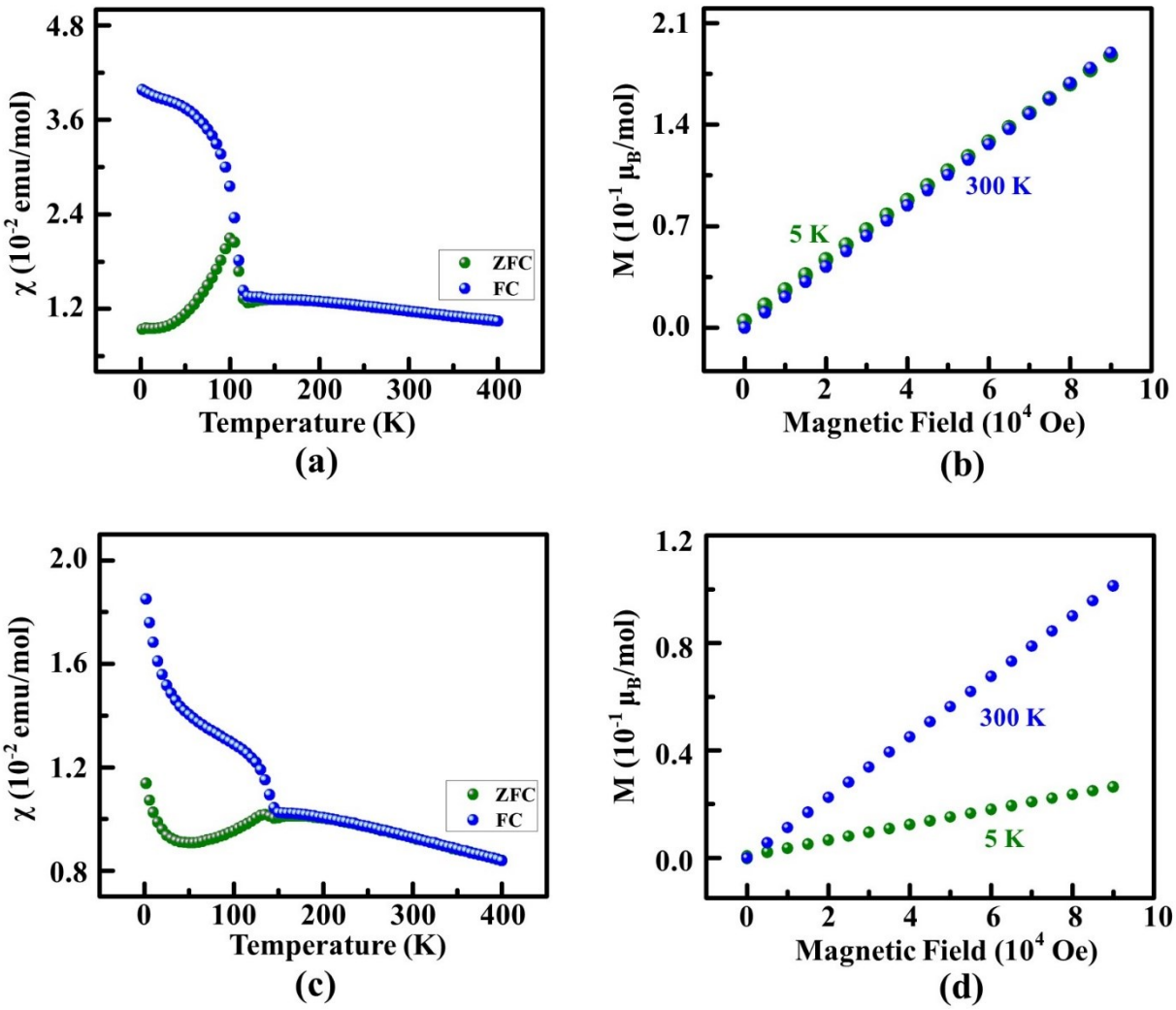

Figure 5. (a) and (b) show magnetic susceptibility and isothermal magnetization data, respectively, for $Ca_3GaMn_2O_8$. Parts (c) and (d) show the data for $SrCa_2GaMn_2O_8$.

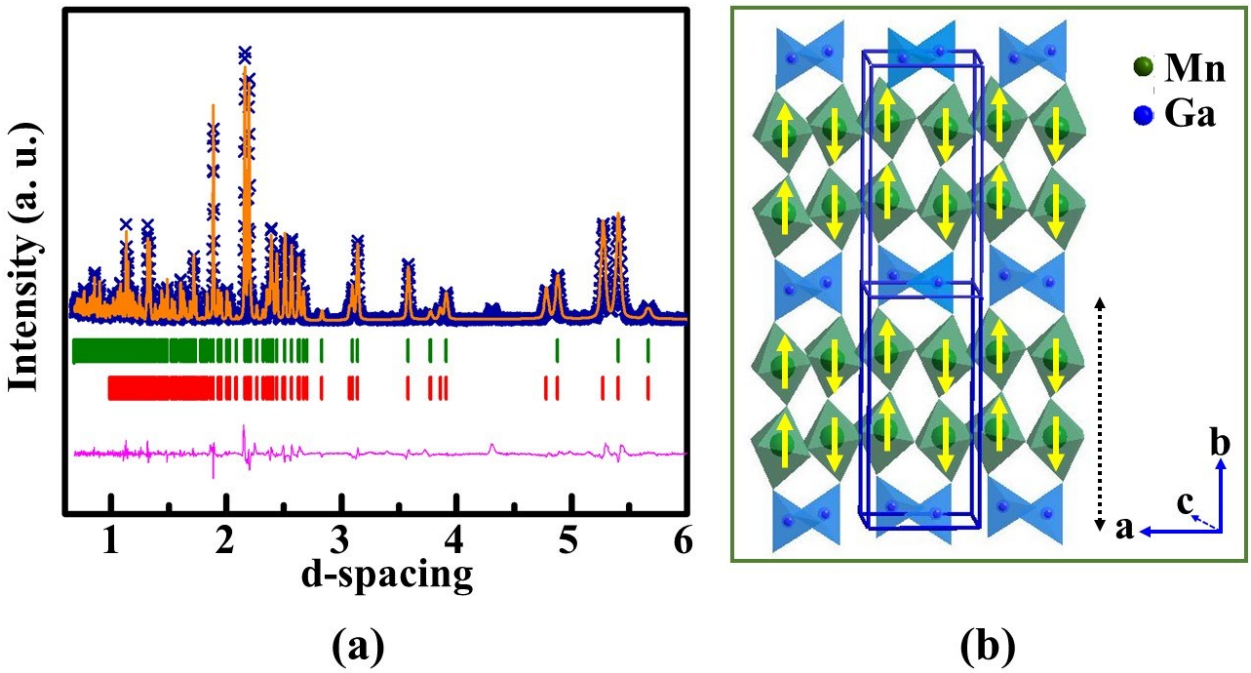

Figure 6. (a) Neutron refinement profile for magnetic (red vertical tick marks) and chemical structure (green vertical tick marks) of $Ca_3GaMn_2O_8$. Small additional peaks at d ≈ 4.3 Å could be due to $CaMnO_{3-\delta}$[30] or MnO[39] that have been reported for similar materials. These small peaks appear when the synthesis is scaled up to gram level (~4 g) for neutron experiments. (b) G-type antiferromagnetic structure of $Ca_3GaMn_2O_8$ with moments along *b* direction.

The magnetic peaks in the neutron scattering pattern could be defined by the same unit cell as that of the chemical structure. The magnetic structure consists of a three-dimensional G-type antiferromagnetic arrangement, where the Mn moments are aligned antiparallel to all nearest neighbors along the b-axis (Figure 6b). The moment of Mn was refined to 3.31(4) μB. This value is lower than the average theoretical moment expected for a 1:1 ratio of Mn^{3+} (d^4) and Mn^{4+} (d^3) cations in $Ca_3GaMn_2O_8$, which is 4.39 μB. However, low moments have been observed for Mn in other Ga-containing oxides such as $Ca_2GaMnO_{5.045}$ (3.6 μB), $SrCaMnGaO_{5+\delta}$ (3.3 μB), and $Sr_2GaMnO_{5.0}$ (3.2 μB).[30, 40-42]

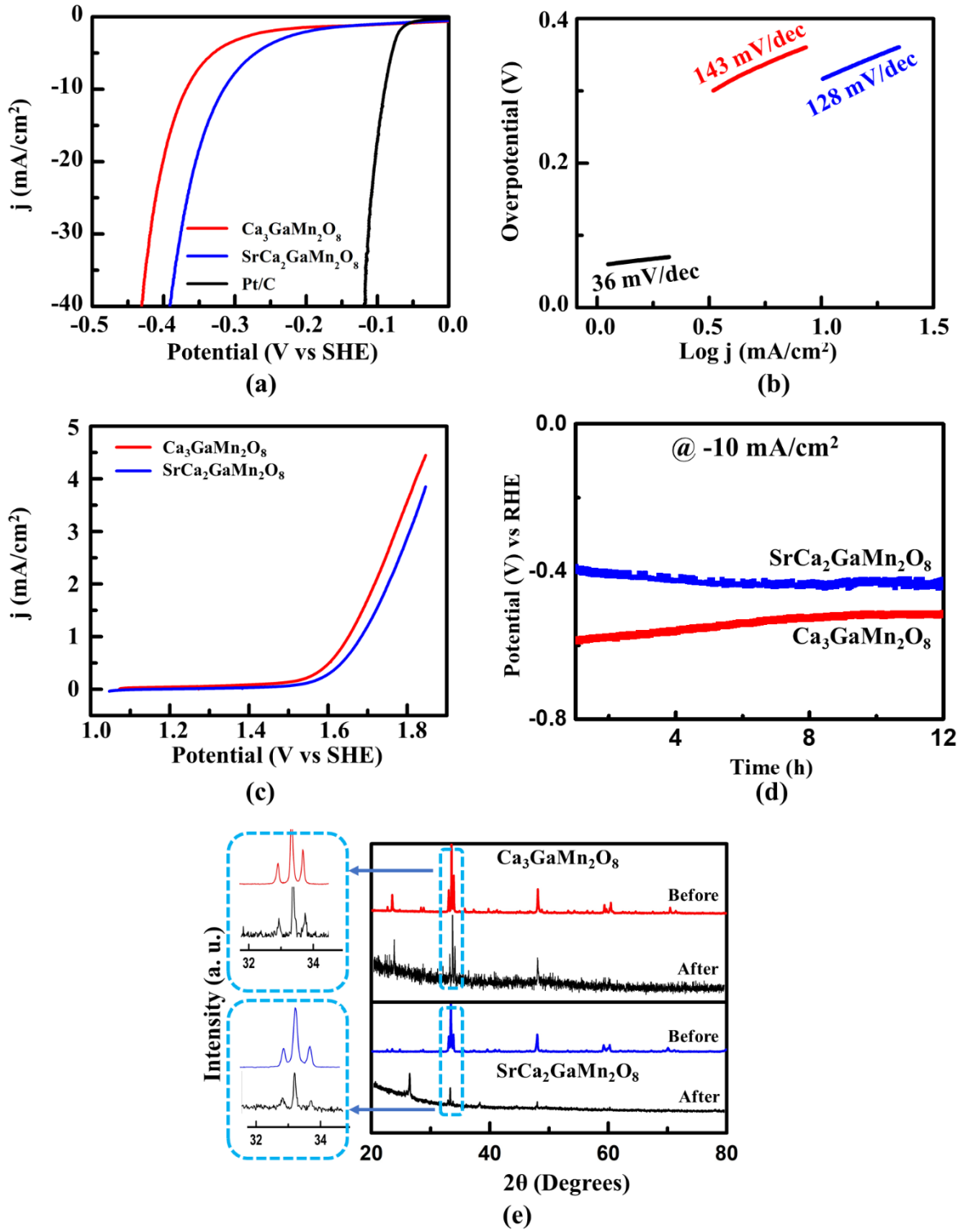

Figure 7. (a) HER activity in 0.5M H_2SO_4. (b) Tafel slopes for HER activity of $Ca_3GaMn_2O_8$ (red), $SrCa_2GaMn_2O_8$ (blue), and Pt/C (black). (c) OER activity in 0.1M KOH. (d) Chronopotentiometry response in 0.5M H_2SO_4 to test the stability during HER. (e) X-ray diffraction data before and after the chronopotentiometry.

3.4. Electrocatalytic Activity for Hydrogen-Evolution Reaction

To our knowledge, the electrocatalytic activity for water splitting has not been studied for this structural family. Therefore, through this work, we introduce another class of materials that can be utilized for water splitting. We investigated the electrocatalytic activity of $Ca_3GaMn_2O_8$ and $SrCa_2GaMn_2O_8$ for hydrogen evolution reaction (HER) and oxygen-evolution reaction (OER) of water splitting process. These compounds showed some degree of OER activity (Figure 7c), but their performance was not high enough to be competitive with existing catalysts. However, remarkably, both materials exhibited very high HER activity, as demonstrated in Figure 7.

For HER studies, the onset potential and overpotential at the current density of 10 mA/cm^2 are used to describe the performance of electrocatalysts.[43-44] Lower values of onset potential and overpotential are indicative of better HER catalysts. The HER studies are often done in either acidic or basic conditions. The basic media (0.1 M or 1 M KOH) did not lead to high activity, but acidic condition (0.5 M H_2SO_4) was found to result in an excellent HER activity for the materials studied here. Figure 7 shows the polarization curves of the two compounds as well as that of the reference electrocatalyst, Pt/C. Clearly, the platinum catalyst shows very good activity, but the high cost of precious metals, such as platinum, is a major problem. There is a substantial ongoing effort toward the discovery of economical HER catalysts.[43-44] Both materials studied in this work show significant HER activity, with an onset potential of ~ -0.27 V for $Ca_3GaMn_2O_8$ and ~ -0.21 V for $SrCa_2GaMn_2O_8$, beyond which the cathodic current increases rapidly. The overpotential (η_{10}) needed to drive a current density of 10 mA/cm^2 is η_{10} ~ -367 mV for $Ca_3GaMn_2O_8$ and η_{10}~ -315 mV for $SrCa_2GaMn_2O_8$. The latter is only ~215 mV higher than that of Pt/C. This is a remarkable performance.

The kinetics of HER can be investigated using the Tafel equation, $\eta = a + b \log j$ [45], where η and j are overpotential and current density, respectively. The slope of η versus $\log j$ plot (Tafel slope) is used to show the relative reaction rates for different catalysts. As shown in Figure 7, the Tafel slopes for $Ca_3GaMn_2O_8$, $SrCa_2GaMn_2O_8$, are 143 mV/dec, and 128 mV/dec, respectively. Chronopotentiometry experiments in 0.5M H_2SO_4 were conducted to test the stability under HER conditions. As shown in Figure 7d, these measurements indicated excellent stability. In addition, X-ray diffraction data (Figure 7e), in particular the largest diagnostic peaks close to 33-34^o (enlarged in the inset), before and after chronopotentiometry showed the retention of the materials structures, further confirming the stability of these compounds. Furthermore, the double layer capacitance, C_{dl}, which is often taken as representative of electrochemically active surface area,[46] was calculated as 127 μF and 649 μF for $Ca_3GaMn_2O_8$ and $SrCa_2GaMn_2O_8$, respectively, matching the trend of HER activity (Figures S1).

It is noted that some oxide electrocatalysts show higher activity than our materials.[43-44] For example, some nano-materials or composites based on metal oxides, such as WO_3 nanosheets (η_{10} ~ -38 mV)[47], MoO_{3-y} nanofilms (η_{10} ~ -201 mV)[48], and WO_3 nanoplates (η_{10} ~ -117 mV)[49], perform better than our compounds in 0.5M H_2SO_4. However, these systems need additional fabrication steps, such as composite formation or nanofabrication. Regarding bulk oxide electrocatalysts, the recently reported $CaSrFeMnO_{6-\delta}$ shows HER catalytic activity with η_{10}~ -310 mV.[6] Nevertheless, the materials studied in this work are still among high performing HER catalysts and show better activity than the extensively studied catalysts MoS_2,[50] gold,[51], and bulk WO_3[52] in acidic condition. In addition, while nanofabricated oxide catalysts for acidic HER, such as those described above, have been reported, perovskite-based oxides, especially in bulk form, that are capable of acidic HER catalysis are uncommon.[6]

3.5. Pseudocapacitive Charge Storage

Another remarkable feature of the materials studied in this work is their pseudocapacitive properties. Supercapacitors have been extensively investigated due to their significant advantages in power density and cycling stability. However, they suffer from low energy density, and their charge storage capacity is limited. Unlike traditional electric double-layer capacitors that rely on non-Faradaic electrostatic charge storage, pseudocapacitors operate based on Faradaic processes, and therefore show greater charge storage capacity.[53] However, since the Faradaic charge transfers in pseudocapacitors occur on or near the surface, they are not limited by bulk diffusion, leading to cyclic voltammetry (CV) and galvanostatic charge-discharge (GCD) behavior similar to traditional capacitors. In theory, pseudocapacitors can possess both high power density of capacitors and high energy density of batteries.[11] Intercalation-based pseudocapacitors involve Faradaic electron transfer that occurs upon intercalation and de-intercalation of ions.[11] The intercalation of oxygen anion was first observed in 1975 in perovskite oxide, $Nd_{1-x}Sr_xCoO_3$, in an alkaline solution.[12] Further utilization of this phenomenon for pseudocapacitive energy storage was shown several decades later in 2014.[11] Since then, some other pseudocapacitive materials based on oxygen anion intercalation have been studied. Examples of the materials that have been investigated are $La_{1-x}Sr_xMnO_3$,[11, 13-14] $La_{1-x}Ca_xMnO_3$,[15] $SrCo_{0.9}Nb_{0.1}O_3$,[16], and $LaNi_{1-x}Fe_xO_{3-\delta}$.[17] The compounds studied before have been primarily perovskite-based oxides, ABO_3, where the A or B sites were occupied by two cations that were distributed randomly. Here, we show that vacancy-ordered systems, such as bilayer structures can also exhibit oxygen-based pseudocapacitive properties.

Figure 8 shows the CVs of $Ca_3GaMn_2O_8$ and $SrCa_2GaMn_2O_8$ in the three-electrode setup at varying scan rates of 5, 20, 40, 60, and 80mV/s in the voltage range of 0.4 to -1.0 V vs Ag/AgCl.

The quasi rectangular CV shapes indicate pseudocapacitive behavior, and Mn^{2+}/Mn^{3+} and Mn^{3+}/Mn^{4+} redox peaks are indicative of the Faradaic processes. [11, 13-17, 54]

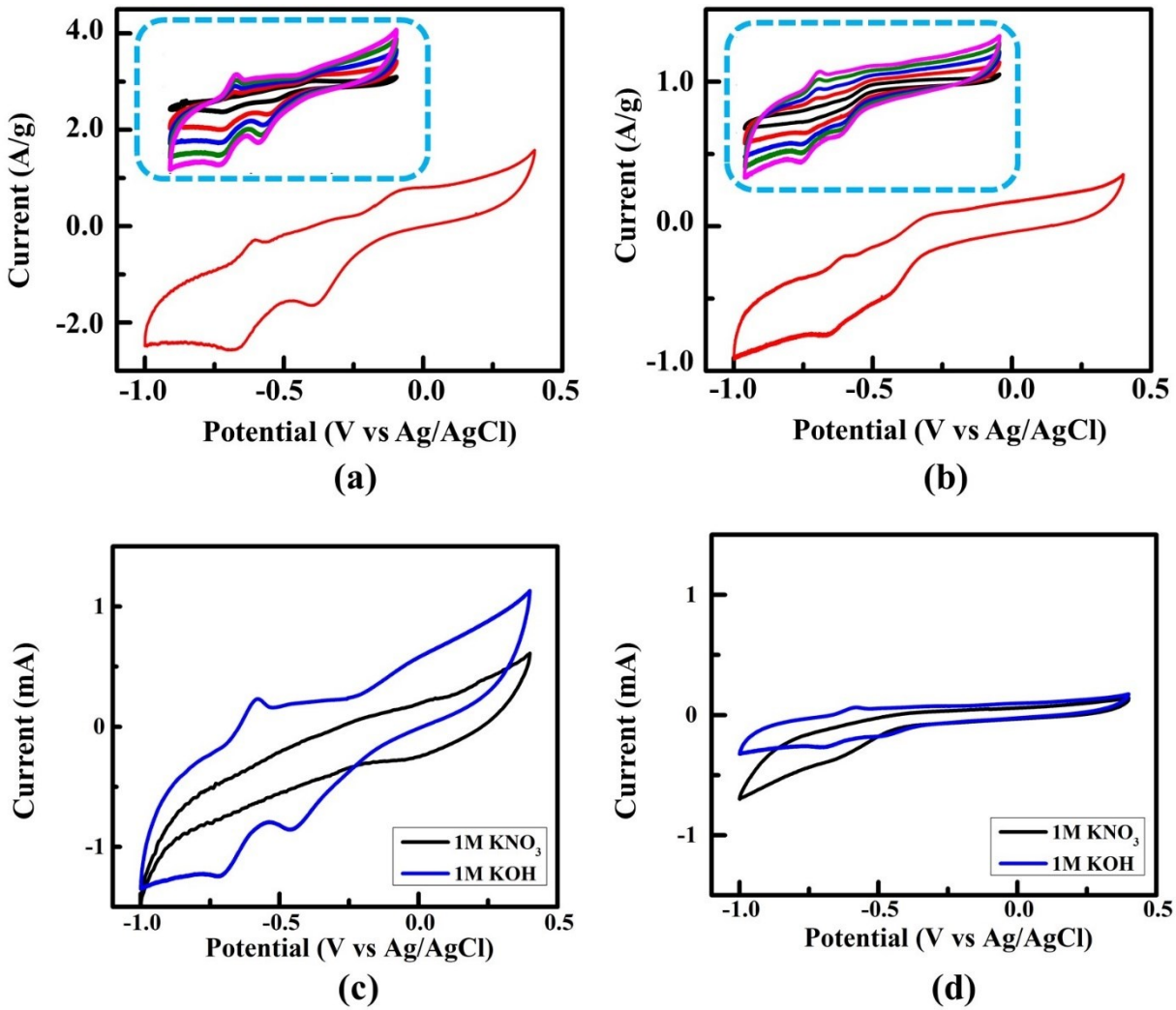

Figure 8. Cyclic voltammetry (CV) curves at 20 mV/s showing the pseudocapacitive properties of (a) $Ca_3GaMn_2O_8$ and (b) $SrCa_2GaMn_2O_8$. The inset shows the CVs at different scan rates, 5, 20, 40, 60, and 80 mV/s in black, red, blue, green, and magenta, respectively. Parts (c) and (d) show the CV curves at 100 mV/s in different electrolytes (KNO_3 and KOH) for $Ca_3GaMn_2O_8$ (c) and $SrCa_2GaMn_2O_8$ (d), respectively.

At a scan rate of 5 mV/s, a pair of oxidation and reduction peaks are observed for both compounds during the anodic and cathodic scans, respectively. These redox peaks become more discernible at faster scan rates as shown in the representative scan rate of 20 mV/s in Figure 8 (a, b). At 5 mV/s, a less intense oxidation peak appears in $Ca_3GaMn_2O_8$ at –0.10 V vs Ag/AgCl (3M NaCl) along with another sharp peak at –0.61 V vs Ag/AgCl (3M NaCl), which are indicative of $Mn^{3+\leftrightarrow 4+}$ and $Mn^{2+\leftrightarrow 3+}$ surface redox reactions, respectively. Similarly, two reduction peaks for this material are observed at –0.35 V and –0.66 V vs Ag/AgCl (3M NaCl) that correspond to the reverse reactions during the cathodic scans. Similarly, for $SrCa_2GaMn_2O_8$, two pairs of oxidation and reduction peaks indicate similar $Mn^{3+\leftrightarrow 4+}$ and $Mn^{2+\leftrightarrow 3+}$ redox events.

As stated before, the peaks are indicative of pseudocapacitive properties, as observed in other pseudocapacitors.[11, 13-15] Examples are the $Mn^{3+/4+}$ and $Mn^{2+/3+}$ oxidation peaks at –0.1 V and –0.3 V vs Hg/HgO for $La_{1-x}Sr_xMnO_{3-\delta}$ (x= 0 – 1) at 10 mV/s (1M KOH),[13] ~ –0.1 V and ~ –0.4 V vs saturated calomel electrode for $La_xSr_{1-x}Cu_{0.1}Mn_{0.9}O_{3-\delta}$ at 10 mV/s (1M KOH),[55] above 0.2 V and ~ –0.1 V vs Hg/HgO for $LaMnO_{2.91}$ at 40 mV/s (1M KOH), [11] and 0.07 V and –0.25 V vs Hg/HgO for $CaMnO_3$ and its Ruddlesden–Popper counterparts at 5 mV/s (1M KOH).[56]

To confirm that these redox processes are dependent on oxygen intercalation facilitated by hydroxide ion, we conducted additional experiments in 1M KNO_3 in the same voltage window (Figure 8c and d), which did not show the redox peaks for any of the two compounds. This indicates that the observed process is dependent on the hydroxide intercalation.[11] As described for other oxygen-based pseudocapacitors,[11, 54] during these surface reactions[14] the intercalated oxygen anion comes from OH^- ion,[54] which loses a proton to another OH^- ion from the electrolyte to produces water,[11] and leaves behind the oxygen ion that is intercalated into the electrode.

At higher scan rates, there is a small shift of the anodic and cathodic peaks to higher and lower potentials, respectively. This shift is commonly observed in pseudocapacitors and is assigned to the internal resistance of the electrode,[57-58] or an indication that the charge transfer kinetics is the limiting step in this process.[59] The peak current increases as a function of increasing the scan rate, which suggests rapid electronic and ionic transport rates.[54, 59] Additionally, while the area changes, the shape of the CV curve remains the same, which indicates enhanced mass transport and electron conduction.[54, 58-59]

The galvanostatic charge-discharge (GCD) behavior of these defect-ordered materials was examined in the potential range of 0.0 to 1.4 V vs Ag/AgCl through the construction of symmetric two-electrode cells, as described in the experimental section. Figure 9a shows the charge/discharge cycles for both materials at the current density of 1 A/g. Also, the GCD curves at various current densities for the best performing material, $Ca_3GaMn_2O_8$, are shown in Figure 9b. The inverted V shape of charge/discharge curves is signature behavior of pseudocapacitors and indicates excellent pseudocapacitive properties for these compounds.[14-15] It is noted that GCD data in batteries, where the processes are controlled by bulk diffusion, do not show the inverted V curves.

The GCD curve can be used to obtain specific capacitance of an electrode at different discharge currents, using equation 4.[53, 60-61]

$$C_s = \frac{4I\,\Delta t}{m\,\Delta V} \text{ or } C_s = \frac{4I}{m\,dV/dt} \qquad (4)$$

where, I is the constant current used for GCD, and dv/dt is the slope of the discharge curve, with ΔV being the voltage window and Δt the discharge time. Also, *m* is the total mass of the active material in both electrodes.[53, 61] Equation 4 may be simplified further by replacing the I/*m* part with current density, *i*, such that mass is not shown in the equation. The multiplier 4 is used to normalize for masses and capacitance of both electrodes and adjust for one electrode. [53, 60-61] Some

researchers use equation 4 without the multiplier 4 [54, 58-59, 62] and take *m* as the mass of the active material in each electrode,[54] although sometimes the meaning of *m* is not explicitly stated.[58-59] In some reports, dv/dt was calculated using two data points on the discharge curve, V_{max} and $1/2V_{max}$,[61-62] to get $dV/dt = (V_{max} - 1/2V_{max})/(t_2-t_1)$,[61-62] where t_2 and t_1 were the discharge times corresponding to V_{max} and $1/2V_{max}$, respectively.[61-62] Equation 4 has also been used to obtain volumetric capacitance, using volume instead of mass.[63]

The C_s values obtained from the GCD curves of our symmetric cells at a current density of 0.5 A/g are 39.2 F/g and 4.5 F/g for $Ca_3GaMn_2O_8$ and $SrCa_2GaMn_2O_8$, respectively. In comparison, a symmetric cell reported using the perovskite $La_{1-x}Sr_xMnO_3$, resulted in the specific capacitance of ~7.75 F/g at 0.5 A/g.[14] Similarly, a symmetric cell based on $La_{1-x}Ca_xMnO_3$ shows the specific capacitance of ~13 F/g at 0.5 A/g,[15] which quickly deteriorates to about 2 F/g.

The energy density of the cell (Wh/Kg) is calculated using the following equation:[64-65]

$$E = \frac{C_s V^2}{2 \times 3.6} \qquad (5)$$

Here, C_s is the specific capacitance and V is the cell voltage window in the GCD curve. The multiplier, $\frac{1}{3.6}$, is needed to obtain the energy density in units of Wh/Kg when the C_s unit is F/g. It is noted that $1F = 1 \frac{s\,A}{V}$ and 1W = 1V × 1A. If the unit of C_s is F/Kg, then the multiplier should also be different, $\frac{1}{3600}$.[60] The latter multiplier has also been used for calculating areal energy density in units of Wh/cm^2 (using areal capacitance)[66-67] and volumetric energy density (using volumetric capacitance) in units of Wh/cm^3.[68] In some cases, researchers have chosen not to show any multipliers, and write the formula as $E = \frac{C_s V^2}{2}$.[11, 69-70] We assume that they have applied the multipliers separately to obtain the right units.

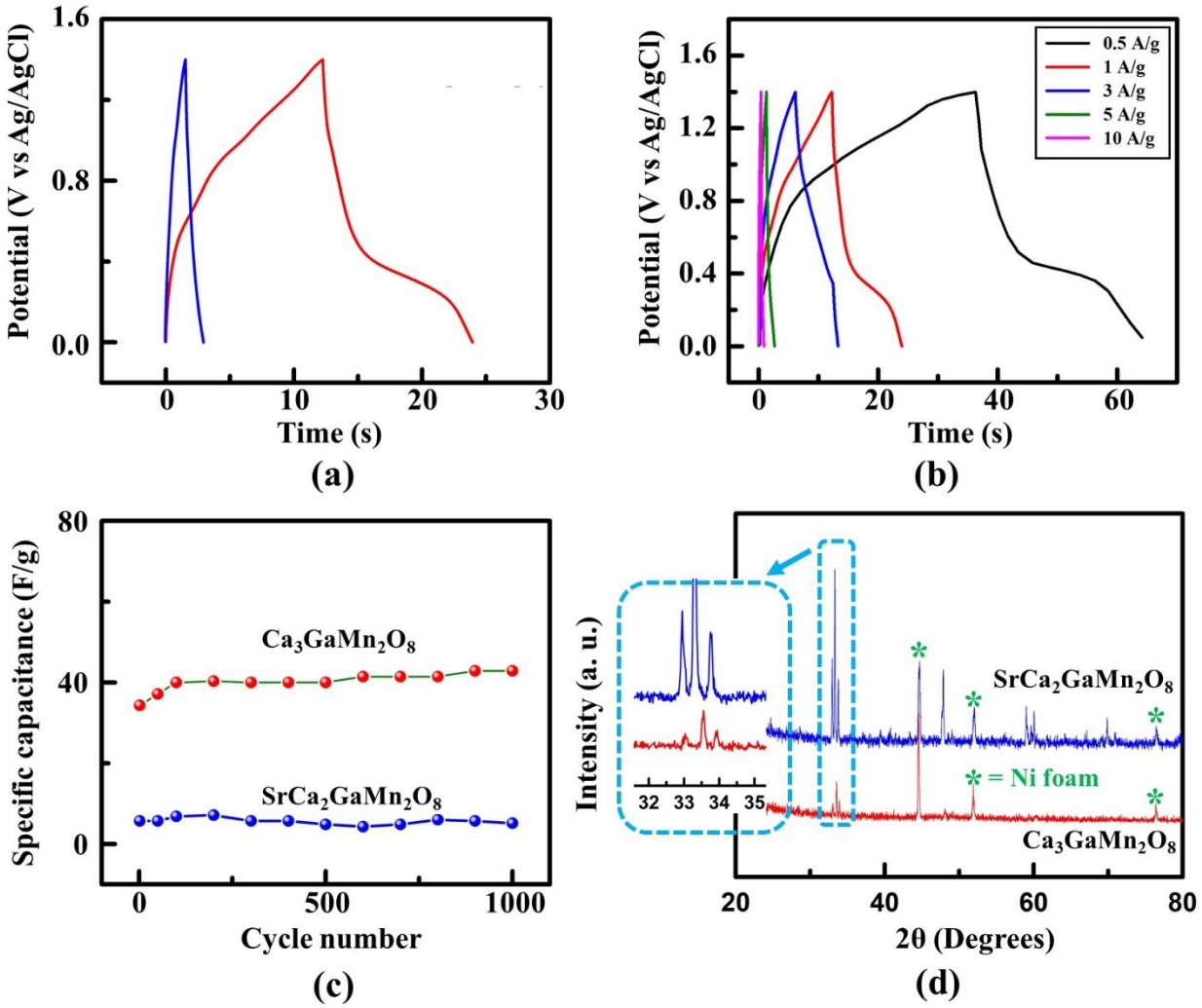

Figure 9. (a) Galvanostatic charge-discharge (GCD) profiles for $Ca_3GaMn_2O_8$ (red) and $SrCa_2GaMn_2O_8$ (blue) at current density of 1 A/g. (b) GDC profiles at various current densities for the best performing material, $Ca_3GaMn_2O_8$. (c) Stability tests up to 1000 cycles. (d) X-ray diffraction data after 1000 GCD cycles.

The power density of the cell (unit: W/Kg) is obtained by dividing the energy density by discharge time, Δt: [64-65]

$$P = \frac{E \times 3600}{\Delta t} \qquad (6)$$

The constant, 3600, is used to obtain the power density in W/Kg when the unit of Δt in seconds, s. [64-65] The same multiplier is used for calculating areal power density (in W/cm^2)[66-67] and volumetric

power density (in W/cm^3).[68] In some cases Δt is expressed in hours (h) with no multiplier.[69-70]

Symmetric cells based on $Ca_3GaMn_2O_8$ and $SrCa_2GaMn_2O_8$ can deliver respective energy densities of 10.69 Wh/Kg and 1.23 Wh/Kg at a power density of 1400 Wkg^{-1}, based on the current density of 0.5A/g. Our best material, $Ca_3GaMn_2O_8$, shows superior energy density and power density compared with many other systems, including a symmetric pseudocapacitor based on $La_{1-x}Sr_xMnO_3$, which has an energy density of ~1.55 Whkg^{-1} with power density less than 1000 Wkg^{-1}, at the current density of 0.5 A/g.[14] Similarly, the symmetric cell reported for $La_{1-x}Ca_xMnO_3$, shows energy density of ~2.6 Whkg^{-1} and power density of ~800 Wkg^{-1} at 0.5 A/g.[15]

Long cycle life is another crucial criterion of a pseudocapacitor for practical applications. Therefore, an endurance test was conducted using GCD cycles at 1 A/g (Figure 9c) for 1000 cycles. Both materials show remarkable retention of specific capacitance after 1000 cycles. The retention of pseudocapacitive properties can be attributed to the high degree of stability of these compounds. Figure 9d shows the X-ray diffraction data of both compounds after 1000 GCD cycles. In particular, the largest peaks close to 33-34^o (enlarged in the inset) are often used as diagnostic peaks for this class of materials. As evident from this figure, both materials retain their structural integrity without the collapse of the material framework or any phase transformation, which leads to a stable pseudocapacitive response. Further stability tests were done for our best pseudocapacitor, $Ca_3GaMn_2O_8$, by repeating 5000 GCD cycles at 10 A/g, as shown in Figure S2, indicating its remarkable stability. The crystallite morphology is also retained after GCD cycles, as shown by SEM images in Figure S3.

Thus, the high energy and power density, combined with outstanding stability, make these defect-ordered materials excellent pseudocapacitors.

CONCLUSIONS

This study highlights the great potential of ordered bilayer systems, an underexplored class of oxides, for electrochemical applications. The simultaneous occurrence of an array of remarkable properties in the same compound is noteworthy. The two materials, $Ca_3GaMn_2O_8$ and $SrCa_2GaMn_2O_8$, are semiconductors in the entire temperature range of 25 – 800 °C, show long-range G-type antiferromagnetic order, and are also capable of catalyzing hydrogen-evolution reaction (HER) of water splitting. They also show excellent pseudocapacitive energy storage with outstanding stability up to 1000 cycles of charge-discharge. The observation of all these properties in this class of materials warrants further studies with the aim of developing active materials for cost-effective and efficient electrochemical applications.

Supporting Information

Graphs of double layer capacitance, further GCD cycles, and SEM images.

Conflicts of interest

The authors declare no conflict of interest.

Acknowledgments

A portion of this research used resources at the Spallation Neutron Source, a DOE Office of Science User Facility operated by the Oak Ridge National Laboratory. This work is supported in part by the National Science Foundation under Grant No. DMR-1943085.

References

1. Wang, H.; Lin, Y.; Liu, S.; Li, J.; Bu, L.; Chen, J.; Xiao, X.; Choi, J.-H.; Gao, L.; Lee, J.-M., Confined growth of pyridinic N–Mo_2C sites on MXenes for hydrogen evolution. *J. Mater. Chem. A,* **2020,** *8*, 7109-7116.
2. Masa, J.; Weide, P.; Peeters, D.; Sinev, I.; Xia, W.; Sun, Z.; Somsen, C.; Muhler, M.; Schuhmann, W., Amorphous Cobalt Boride (Co_2B) as a Highly Efficient Nonprecious Catalyst for Electrochemical Water Splitting: Oxygen and Hydrogen Evolution. *Adv. Energy Mater.* **2016,** *6*, 1502313.
3. Wang, H.; Xiao, X.; Liu, S.; Chiang, C.-L.; Kuai, X.; Peng, C.-K.; Lin, Y.-C.; Meng, X.; Zhao, J.; Choi, J.; Lin, Y.-G.; Lee, J.-M.; Gao, L., Structural and Electronic Optimization of MoS_2 Edges for Hydrogen Evolution. *J. Am. Chem. Soc.* **2019,** *141*, 18578-18584.
4. Prabhu, P.; Jose, V.; Lee, J.-M., Design Strategies for Development of TMD-Based Heterostructures in Electrochemical Energy Systems. *Matter* **2020,** *2*, 526-553.
5. Sultana, U. K.; Riches, J. D.; O'Mullane, A. P., Gold Doping in a Layered Co-Ni Hydroxide System via Galvanic Replacement for Overall Electrochemical Water Splitting. *Adv. Funct. Mater.* **2018,** *28*, 1804361.
6. Hona, R. K.; Karki, S. B.; Ramezanipour, F., Oxide Electrocatalysts Based on Earth-Abundant Metals for Both Hydrogen- and Oxygen-Evolution Reactions. *ACS Sustainable Chem. Eng.* **2020,** *8*, 11549-11557.
7. Hona, R. K.; Ramezanipour, F., Remarkable Oxygen-Evolution Activity of a Perovskite Oxide from the $Ca_{2-x}Sr_xFe_2O_{6-\delta}$ Series. *Angew. Chem.* **2019,** *58*, 2060-2063.
8. Suntivich, J.; May, K. J.; Gasteiger, H. A.; Goodenough, J. B.; Shao-Horn, Y., A Perovskite Oxide Optimized for Oxygen Evolution Catalysis from Molecular Orbital Principles. *Science* **2011,** *334*, 1383.
9. Zhang, W.; Jia, Q.; Liang, H.; Cui, L.; Wei, D.; Liu, J., Iron doped Ni_3S_2 nanorods directly grown on $FeNi_3$ foam as an efficient bifunctional catalyst for overall water splitting. *Chem. Eng. J.* **2020,** *396*, 125315.
10. Li, X.; Zhang, R.; Luo, Y.; Liu, Q.; Lu, S.; Chen, G.; Gao, S.; Chen, S.; Sun, X., A cobalt–phosphorus nanoparticle decorated N-doped carbon nanosheet array for efficient and durable hydrogen evolution at alkaline pH. *Sustain. Energy Fuels* **2020,** *4*, 3884-3887.
11. Mefford, J. T.; Hardin, W. G.; Dai, S.; Johnston, K. P.; Stevenson, K. J., Anion charge storage through oxygen intercalation in $LaMnO_3$ perovskite pseudocapacitor electrodes. *Nat. Mater.* **2014,** *13*, 726.
12. Kudo, T.; Obayashi, H.; Gejo, T., Electrochemical Behavior of the Perovskite-Type $Nd_{1-x}Sr_x CoO_3$ in an Aqueous Alkaline Solution. *J. Electrochem. Soc. 1* **1975,** *122*, 159-163.
13. Alexander, C. T.; Mefford, J. T.; Saunders, J.; Forslund, R. P.; Johnston, K. P.; Stevenson, K. J., Anion-Based Pseudocapacitance of the Perovskite Library $La_{1-x}Sr_xBO_{3-\delta}$ (B = Fe, Mn, Co). *ACS Appl. Mater. Interfaces* **2019,** *11*, 5084-5094.
14. Lang, X.; Mo, H.; Hu, X.; Tian, H., Supercapacitor performance of perovskite $La_{1-x}Sr_xMnO_3$. *Dalton Trans.* **2017,** *46*, 13720-13730.
15. Mo, H.; Nan, H.; Lang, X.; Liu, S.; Qiao, L.; Hu, X.; Tian, H., Influence of calcium doping on performance of $LaMnO_3$ supercapacitors. *Ceram. Int.* **2018,** *44*, 9733-9741.
16. Zhu, L.; Liu, Y.; Su, C.; Zhou, W.; Liu, M.; Shao, Z., Perovskite $SrCo_{0.9}Nb_{0.1}O_{3-\delta}$ as an Anion-Intercalated Electrode Material for Supercapacitors with Ultrahigh Volumetric Energy Density. *Angew. Chem., Int. Ed.* **2016,** *55*, 9576-9579.
17. Alexander, C. T.; Forslund, R. P.; Johnston, K. P.; Stevenson, K. J., Tuning Redox Transitions via the Inductive Effect in $LaNi_{1-x}Fe_xO_{3-\delta}$ Perovskites for High-Power Asymmetric and Symmetric Pseudocapacitors. *ACS Appl. Energy Mater.* **2019,** *2*, 6558-6568.
18. Hona, R. K.; Huq, A.; Mulmi, S.; Ramezanipour, F., Transformation of Structure, Electrical Conductivity, and Magnetism in $AA'Fe_2O_{6-\delta}$, A = Sr, Ca and A′ = Sr. *Inorg. Chem.* **2017,** *56*, 9716-9724.
19. Hona, R. K.; Ramezanipour, F., Enhanced electrical properties in $BaSrFe_2O_{6-\delta}$ ($\delta = 0.5$): A disordered defect-perovskite. *Polyhedron* **2019,** *167*, 69-74.

20. Hona, R. K.; Huq, A.; Ramezanipour, F., Unraveling the Role of Structural Order in the Transformation of Electrical Conductivity in $Ca_2FeCoO_{6-\delta}$, $CaSrFeCoO_{6-\delta}$, and $Sr_2FeCoO_{6-\delta}$. *Inorg. Chem.* **2017,** *56*, 14494-14505.
21. Reehuis, M.; Ulrich, C.; Maljuk, A.; Niedermayer, C.; Ouladdiaf, B.; Hoser, A.; Hofmann, T.; Keimer, B., Neutron diffraction study of spin and charge ordering in $SrFeO_{3-\delta}$. *Phys. Rev. B* **2012,** *85*, 184109.
22. Karki, S. B.; Hona, R. K.; Ramezanipour, F., Effect of Structure on Sensor Properties of Oxygen-Deficient Perovskites, $A_2BB'O_5$ (A = Ca, Sr; B = Fe; B′ = Fe, Mn) for Oxygen, Carbon Dioxide and Carbon Monoxide Sensing. *J. Electron. Mater.* **2020,** *49*, 1557-1567.
23. Grenier, J.-C.; Darriet, J.; Pouchard, M.; Hagenmuller, P., Mise en evidence d'une nouvelle famille de phases de type perovskite lacunaire ordonnee de formule $A_3M_3O_8$ ($AMO_{2,67}$). *Mater. Res. Bull.* **1976,** *11*, 1219-1225.
24. Hudspeth, J. M.; Goossens, D. J.; Studer, A. J.; Withers, R. L.; Norén, L., The crystal and magnetic structures of $LaCa_2Fe_3O_8$ and $NdCa_2Fe_3O_8$. *J. Phys. Condens. Matter* **2009,** *21*, 124206.
25. Luo, K.; Hayward, M. A., The synthesis and characterisation of $LaCa_2Fe_2GaO_8$. *J. Solid State Chem.* **2013,** *198*, 203-209.
26. Battle, P. D.; Gibb, T. C.; Lightfoot, P., The crystal and magnetic structures of $Sr_2LaFe_3O_8$. *J. Solid State Chem.* **1990,** *84*, 237-244.
27. Martínez de Irujo-Labalde, X.; Goto, M.; Urones-Garrote, E.; Amador, U.; Ritter, C.; Amano Patino, M. E.; Koedtruad, A.; Tan, Z.; Shimakawa, Y.; García-Martín, S., Multiferroism Induced by Spontaneous Structural Ordering in Antiferromagnetic Iron Perovskites. *Chem. Mater.* **2019,** *31*, 5993-6000.
28. Yusuf, S. M.; De Teresa, J. M.; Algarabel, P. A.; Mukadam, M. D.; Mirebeau, I.; Mignot, J. M.; Marquina, C.; Ibarra, M. R., Two- and three-dimensional magnetic ordering in the bilayer manganite $Ca_{2.5}Sr_{0.5}GaMn_2O_8$. *Phys. Rev. B* **2006,** *74*, 184409.
29. Bera, A. K.; Yusuf, S. M., Ferromagnetic clusters in the Brownmillerite bilayered compounds $Ca_{2.5-x}La_xSr_{0.5}GaMn_2O_8$: An approach to achieve layered spintronics materials. *J. Appl. Phys.* **2010,** *107*, 013911.
30. Battle, P. D.; Blundell, S. J.; Santhosh, P. N.; Rosseinsky, M. J.; Steer, C., Electronic phase transitions and magnetoresistance in a new bilayer manganate, $Ca_{2.5}Sr_{0.5}GaMn_2O_8$. *J. Phys. Condens. Matter* **2002,** *14*, 13569-13577.
31. Larson, A. C.; Von Dreele, R. B. *General Structure Analysis System (GSAS)*; Los Alamos National Laboratory: Los Alamos, NM: 1994.
32. Toby, B. H., EXPGUI, a graphical user interface for GSAS. . *J. Appl. Crystallogr.* **2001,** *34*, 210−213.
33. Jeerage, K. M.; Candelaria, S. L.; Stavis, S. M., Rapid Synthesis and Correlative Measurements of Electrocatalytic Nickel/Iron Oxide Nanoparticles. *Sci. Rep.* **2018,** *8* (1), 4584.
34. Jia, Y.; Zhang, L.; Du, A.; Gao, G.; Chen, J.; Yan, X.; Brown, C. L.; Yao, X., Defect Graphene as a Trifunctional Catalyst for Electrochemical Reactions. *Adv. Mater.* **2016,** *28*, 9532-9538.
35. Karki, S. B.; Ramezanipour, F., Magnetic and electrical properties of $BaSrMMoO_6$ (M = Mn, Fe, Co, and Ni). *Mater. Today Chem.* **2019,** *13*, 25-33.
36. Asenath-Smith, E.; Lokuhewa, I. N.; Misture, S. T.; Edwards, D. D., p-Type thermoelectric properties of the oxygen-deficient perovskite $Ca_2Fe_2O_5$ in the brownmillerite structure. *J. Solid State Chem.* **2010,** *183*, 1670-1677.
37. Patrakeev, M. V.; Leonidov, I. A.; Kozhevnikov, V. L.; Poeppelmeier, K. R., p-Type electron transport in $La_{1-x}Sr_xFeO_{3-\delta}$ at high temperatures. *J. Solid State Chem.* **2005,** *178*, 921-927.
38. Mineshige, A.; Inaba, M.; Yao, T.; Ogumi, Z.; Kikuchi, K.; Kawase, M., Crystal Structure and Metal–Insulator Transition of $La_{1-x}Sr_xCoO_3$. *J. Solid State Chem.* **1996,** *121*, 423-429.
39. Li, M.-R.; Hodges, J. P.; Retuerto, M.; Deng, Z.; Stephens, P. W.; Croft, M. C.; Deng, X.; Kotliar, G.; Sánchez-Benítez, J.; Walker, D.; Greenblatt, M., Mn_2MnReO_6: Synthesis and Magnetic Structure

Determination of a New Transition-Metal-Only Double Perovskite Canted Antiferromagnet. *Chem. Mater.* **2016,** *28*, 3148-3158.
40. Sheptyakov, D. V.; Abakumov, A. M.; Antipov, E. V.; Balagurov, A. M.; Billinge, S. J. L.; Fischer, P.; Keller, L.; Lobanov, M. V.; Pavlyuk, B. P.; Pomjakushin, V. Y.; Rozova, M. G., Crystal and magnetic structures of new layered oxides A_2GaMnO_{5+y} (A=Ca, Sr). *Appl. Phys. A* **2002,** *74*, s1734-s1736.
41. Battle, P. D.; Bell, A. M. T.; Blundell, S. J.; Coldea, A. I.; Gallon, D. J.; Pratt, F. L.; Rosseinsky, M. J.; Steer, C. A., Crystal Structure and Magnetic Properties of $SrCaMnGaO_{5+\delta}$. *J. Solid State Chem.* **2002,** *167*, 188-195.
42. Wright, A. J.; Palmer, H. M.; Anderson, P. A.; Greaves, C., Structures and magnetic ordering in the brownmillerite phases, Sr_2MnGaO_5 and Ca_2MnAlO_5. *J. Mater. Chem.* **2002,** *12*, 978-982.
43. Wang, J.; Gao, Y.; Chen, D.; Liu, J.; Zhang, Z.; Shao, Z.; Ciucci, F., Water Splitting with an Enhanced Bifunctional Double Perovskite. *ACS Catal.* **2018,** *8*, 364-371.
44. Xu, X.; Chen, Y.; Zhou, W.; Zhu, Z.; Su, C.; Liu, M.; Shao, Z., A Perovskite Electrocatalyst for Efficient Hydrogen Evolution Reaction. *Adv. Mater.* **2016,** *28*, 6442-6448.
45. Oh, S.; Kim, H.; Kwon, Y.; Kim, M.; Cho, E.; Kwon, H., Porous Co–P foam as an efficient bifunctional electrocatalyst for hydrogen and oxygen evolution reactions. *J. Mater. Chem. A* **2016,** *4*, 18272-18277.
46. Pan, Y.; Chen, Y.; Li, X.; Liu, Y.; Liu, C., Nanostructured nickel sulfides: phase evolution, characterization and electrocatalytic properties for the hydrogen evolution reaction. *RSC Adv.* **2015,** *5*, 104740-104749.
47. Zheng, T.; Sang, W.; He, Z.; Wei, Q.; Chen, B.; Li, H.; Cao, C.; Huang, R.; Yan, X.; Pan, B.; Zhou, S.; Zeng, J., Conductive Tungsten Oxide Nanosheets for Highly Efficient Hydrogen Evolution. *Nano Lett.* **2017,** *17*, 7968-7973.
48. Zhang, W.; Li, H.; Firby, C. J.; Al-Hussein, M.; Elezzabi, A. Y., Oxygen-Vacancy-Tunable Electrochemical Properties of Electrodeposited Molybdenum Oxide Films. *ACS Appl. Mater. Interfaces* **2019,** *11*, 20378-20385.
49. Han, H.; Nayak, A. K.; Choi, H.; Ali, G.; Kwon, J.; Choi, S.; Paik, U.; Song, T., Partial Dehydration in Hydrated Tungsten Oxide Nanoplates Leads to Excellent and Robust Bifunctional Oxygen Reduction and Hydrogen Evolution Reactions in Acidic Media. *ACS Sustainable Chem. Eng.* **2020,** *8*, 9507-9518.
50. Guo, X.; Tong, X.; Wang, Y.; Chen, C.; Jin, G.; Guo, X.-Y., High photoelectrocatalytic performance of a MoS_2–SiC hybrid structure for hydrogen evolution reaction. *J. Mater. Chem. A* **2013,** *1*, 4657-4661.
51. Uosaki, K.; Elumalai, G.; Dinh, H. C.; Lyalin, A.; Taketsugu, T.; Noguchi, H., Highly Efficient Electrochemical Hydrogen Evolution Reaction at Insulating Boron Nitride Nanosheet on Inert Gold Substrate. *Sci. Rep.* **2016,** *6*, 32217.
52. Li, Y. H.; Liu, P. F.; Pan, L. F.; Wang, H. F.; Yang, Z. Z.; Zheng, L. R.; Hu, P.; Zhao, H. J.; Gu, L.; Yang, H. G., Local atomic structure modulations activate metal oxide as electrocatalyst for hydrogen evolution in acidic water. *Nat. Commun.* **2015,** *6*, 8064.
53. Vellacheri, R.; Al-Haddad, A.; Zhao, H.; Wang, W.; Wang, C.; Lei, Y., High performance supercapacitor for efficient energy storage under extreme environmental temperatures. *Nano Energy* **2014,** *8*, 231-237.
54. Che, W.; Wei, M.; Sang, Z.; Ou, Y.; Liu, Y.; Liu, J., Perovskite $LaNiO_{3-\delta}$ oxide as an anion-intercalated pseudocapacitor electrode. *J. Alloys Compd.* **2018,** *731*, 381-388.
55. Cao, Y.; Lin, B.; Sun, Y.; Yang, H.; Zhang, X., Synthesis, structure and electrochemical properties of lanthanum manganese nanofibers doped with Sr and Cu. *J. Alloys Compd.* **2015,** *638*, 204-213.
56. Forslund, R. P.; Pender, J.; Alexander, C. T.; Johnston, K. P.; Stevenson, K. J., Comparison of perovskite and perovskite derivatives for use in anion-based pseudocapacitor applications. *J. Mater. Chem. A* **2019,** *7*, 21222-21231.
57. Yan, J.; Fan, Z.; Sun, W.; Ning, G.; Wei, T.; Zhang, Q.; Zhang, R.; Zhi, L.; Wei, F., Advanced Asymmetric Supercapacitors Based on $Ni(OH)_2$/Graphene and Porous Graphene Electrodes with High Energy Density. *Adv. Funct. Mater.* **2012,** *22*, 2632-2641.

58. Zhang, J.; Liu, H.; Shi, P.; Li, Y.; Huang, L.; Mai, W.; Tan, S.; Cai, X., Growth of nickel (111) plane: The key role in nickel for further improving the electrochemical property of hexagonal nickel hydroxide-nickel & reduced graphene oxide composite. *J. Power Sources* **2014,** *267*, 356-365.
59. Guo, D.; Zhang, H.; Yu, X.; Zhang, M.; Zhang, P.; Li, Q.; Wang, T., Facile synthesis and excellent electrochemical properties of $CoMoO_4$ nanoplate arrays as supercapacitors. *J. Mater. Chem. A* **2013,** *1*, 7247-7254.
60. Béguin, F.; Presser, V.; Balducci, A.; Frackowiak, E., Carbons and Electrolytes for Advanced Supercapacitors. *Adv. Mater.* **2014,** *26*, 2219-2251.
61. Stoller, M. D.; Ruoff, R. S., Best practice methods for determining an electrode material's performance for ultracapacitors. *Energy Environ. Sci.* **2010,** *3*, 1294-1301.
62. Zhang, J.; Zhao, X. S., On the Configuration of Supercapacitors for Maximizing Electrochemical Performance. *ChemSusChem* **2012,** *5*, 818-841.
63. Wang, G.; Kim, S.-K.; Wang, M. C.; Zhai, T.; Munukutla, S.; Girolami, G. S.; Sempsrott, P. J.; Nam, S.; Braun, P. V.; Lyding, J. W., Enhanced Electrical and Mechanical Properties of Chemically Cross-Linked Carbon-Nanotube-Based Fibers and Their Application in High-Performance Supercapacitors. *ACS Nano* **2020,** *14*, 632-639.
64. Kshetri, T.; Tran, D. T.; Nguyen, D. C.; Kim, N. H.; Lau, K.-t.; Lee, J. H., Ternary graphene-carbon nanofibers-carbon nanotubes structure for hybrid supercapacitor. *Chem. Eng. J.* **2020,** *380*, 122543.
65. Balamurugan, J.; Thanh, T. D.; Kim, N. H.; Lee, J. H., Facile synthesis of 3D hierarchical N-doped graphene nanosheet/cobalt encapsulated carbon nanotubes for high energy density asymmetric supercapacitors. *J. Mater. Chem. A* **2016,** *4*, 9555-9565.
66. da Silva, R. J.; Lima, R. M. A. P.; de Oliveira, M. C. A.; Alcaraz-Espinoza, J. J.; de Melo, C. P.; de Oliveira, H. P., Supercapacitors based on (carbon nanostructure)/PEDOT/(eggshell membrane) electrodes. *J. Electroanal. Chem.* **2020,** *856*, 113658.
67. Alcaraz-Espinoza, J. J.; de Oliveira, H. P., Flexible supercapacitors based on a ternary composite of polyaniline/polypyrrole/graphite on gold coated sandpaper. *Electrochim. Acta* **2018,** *274*, 200-207.
68. Yu, D.; Goh, K.; Wang, H.; Wei, L.; Jiang, W.; Zhang, Q.; Dai, L.; Chen, Y., Scalable synthesis of hierarchically structured carbon nanotube–graphene fibres for capacitive energy storage. *Nat. Nanotechnol.* **2014,** *9*, 555-562.
69. Kim, B. K.; Sy, S.; Yu, A.; Zhang, J., Electrochemical Supercapacitors for Energy Storage and Conversion. In *Handbook of Clean Energy Systems*, Wiley, 2015: pp 1-25.
70. Bag, S.; Raj, C. R., Facile shape-controlled growth of hierarchical mesoporous δ-MnO_2 for the development of asymmetric supercapacitors. *J. Mater. Chem. A* **2016,** *4*, 8384-8394.

For Table of Contents Only: